Weierstraß-Institut

für Angewandte Analysis und Stochastik

Leibniz-Institut im Forschungsverbund Berlin e. V.

Technical Report ISSN 1618 – 7776

Mathematical modeling and numerical simulations of diode lasers with micro-integrated external resonators

Mindaugas Radziunas[1]

submitted: 31 March, 2016

[1] Weierstrass Institute
Mohrenstr. 39
10117 Berlin
Germany
E-Mail: Mindaugas.Radziunas@wias-berlin.de

No. 15

Berlin 2016

2010 *Mathematics Subject Classification.* 78A60, 35Q60, 35B30, 78-05.

2008 *Physics and Astronomy Classification Scheme.* 42.55.Px, 42.65.bc, 42.60.Pk, 42.60.Mi.

Key words and phrases. External cavity diode laser, simulations, analysis, experiments, software, model.

Edited by
Weierstraß-Institut für Angewandte Analysis und Stochastik (WIAS)
Leibniz-Institut im Forschungsverbund Berlin e. V.
Mohrenstraße 39
10117 Berlin
Germany

Fax: +49 30 20372-303
E-Mail: preprint@wias-berlin.de
World Wide Web: http://www.wias-berlin.de/

Abstract

This report summarizes our scientific activities within the project MANUMIEL (BMBF Program “Förderung der Wissenschaftlich-Technologischen Zusammenarbeit (WTZ) mit der Republik Moldau”, FKZ 01DK13020A). Namely, we discuss modeling of external cavity diode lasers, numerical simulations and analysis of these devices using the software package `LDSL-tool`, as well as the development of this software.

1 Introduction

This is the final report of the project MANUMIEL (01.10.13-30.09.15) in the frame of the BMBF Program "Förderung der Wissenschaftlich-Technologischen Zusammenarbeit (WTZ) mit der Republik Moldau", FKZ 01DK13020A.

The goal of the project was to establish a German - Moldavian cooperation for the theoretical investigation of the dynamics of micro-integrated external-cavity diode lasers (ECDLs). The micro-integrated ECDL schematically shown in Fig. 1 consists of an active section (S_a), an extended external volume holographic Bragg grating (BG, S_b), and a glass lens (S_l) closely located at the inner facet of the active section. Two air gaps $S_{g'}$ and $S_{g''}$ separate the active section from the lens and the lens from the BG, respectively. All parts are micro-integrated on an AlN ceramic base plate (micro-optical bench) with a footprint of only $25 \times 80\,\mathrm{mm}^2$. The resonator is formed between the outer facet of the active section and the BG. The ECDL devices are designed for

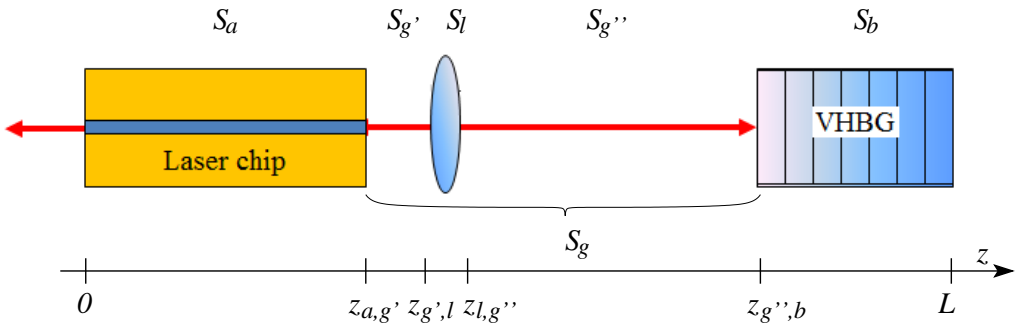

Figure 1: Schematic representation of the ECDL device.

quantum optical experiments in space. These lasers demonstrate a complex non-linear electro-optic behavior which is not completely understood yet. The MANUMIEL project has stimulated the development of the mathematical modeling and numerical simulations of ECDLs at the Technical University of Moldova (TUM).

The theoretical investigations and measurements of the ECDLs done by the colleagues from the TUM and the Ferdinand-Braun-Institut, Leibniz-Institut für Höchstfrequenztechnik (FBH), respectively, have contributed to a better understanding of the observed phenomena and help to improve the design of ECDLs. The simulations and analysis of ECDLs were relying on the

software package LDSL-tool [1] developed at the Weierstrass Institute. During this project, a further development of this software was performed. Namely, at the Weierstrass Institute we have implemented a MATLAB-based user interface (parallel to an existing RLaB-based interface), which can make our software a more attractive tool for a wider range of potential users. We have also developed a new multi-mode delay differential equation model suited for simulations and analysis of diode lasers with external cavities such as ECDL devices.

2 Traveling wave modeling of the ECDLs

During recent years the control and stabilization of laser emission of semiconductor lasers (SLs) by an external cavity has received considerable attention. In particular, the integration of a Bragg grating into the laser cavity allows a stabilization of the emission wavelength as required by many applications such as frequency conversion, quantum-optical experiments and coherent optical communication. Recently, a novel micro-integration approach was used to build a compact, narrow linewidth External Cavity Diode Laser (ECDL) with a volume holographic Bragg grating [2] ideally suited for quantum-optical experiments in space.

Semiconductor lasers subject to the delayed optical feedback from a distant mirror have been investigated extensively during the past two decades. Different dynamic regimes, including continuous-wave (cw) states, periodic and quasi-periodic pulsations, low frequency fluctuations, and a coherent collapse were examined (see Ref. [3] and references therein). The simplest method for modeling a semiconductor laser with a *weak* optical feedback is given by the Lang-Kobayashi (LK) model [4], which is a rate equation based system of delayed differential equations. Although it is relatively simple, the LK model admits a reasonable qualitative agreement with experiments and, therefore, provides a good understanding of nonlinear dynamics in the considered device [5]. The LK modeling approach was also successfully used to get a deep understanding of the stabilization or destabilization of the cw state by different configurations of the external cavity [6, 7].

On the other hand, the LK model is mostly suited for the study of laser systems with small optical feedback and large ratio between the lengths of the external cavity and the laser, such that the length of the emitter itself can be neglected. A more appropriate way to describe the dynamics of semiconductor lasers with a *short* external cavity is given by the Traveling Wave (TW) model, which is a partial differential equation model that includes the spatial (longitudinal) distribution of the fields [8, 9]. This model is well suited not only for simulations of ECDL devices, but also for a detailed study of coexisting stationary states [7] determined by longitudinal modes [10], and for numerical continuation and bifurcation analysis [11]. In this section of our report we apply the TW model for the investigation of the dynamics of the ECDL device.

2.1 Model equations

It is assumed, that the TW equations

$$\frac{n_g}{c_0}\partial_t E^{\pm} = \left[\mp\partial_z - i\beta(N,I)\right] E^{\pm} - i\kappa E^{\mp} + F_{sp}^{\pm} \tag{1}$$

govern the dynamics of the slowly varying complex amplitudes $E^+(z,t)$ and $E^-(z,t)$ of the counter-propagating optical fields within each part of the laser. Here, c_0 is the speed of light in vacuum, $F_{sp}^{\pm}$ is the stochastic spontaneous emission term in the active section S_a, and n_g is the group index (different within different parts of the device).

At the output ports of the ECDL ($z=0$ and $z=L$) as well as at the interfaces $z=z_{k,j}$ of the adjacent parts S_k and S_j of the device where $k,j \in \{a,g',l,g'',b\}$ (see Fig. 1), the complex optical fields are related by the following reflection/transmission conditions [10]:

$$\begin{array}{ll} E^+(0,t) & = -r_0^* E^-(0,t), \qquad E^-(L,t) = r_L E^+(L,t), \\ E^+(z_{k,j}^+,t) & = -r_{k,j}^* E^-(z_{k,j}^+,t) + t_{k,j} E^+(z_{k,j}^-,t), \\ E^-(z_{k,j}^-,t) & = r_{k,j} E^+(z_{k,j}^-,t) + t_{k,j} E^-(z_{k,j}^+,t). \end{array} \tag{2}$$

Here $z_{k,j}^-$ and $z_{k,j}^+$ denote the left and the right sides of the section interface, whereas $r_{k,j}$ and $t_{k,j} = \sqrt{1-|r_{k,j}|^2}$ are the field amplitude reflectivity and transmission coefficients.

The relative propagation factor β is given by

$$\beta = \delta - i\frac{\alpha}{2} - i\frac{\mathcal{D}}{2} + \delta_T(I) + i\frac{(1+i\alpha_H)\Gamma g'\,(N-N_{tr})}{2}. \tag{3}$$

Outside the active section S_a the only non-vanishing terms in the expression (3) can be the internal loss constant α and the field phase tuning δ. In the absence of the field reflections at the edges of the lens ($r_{g',l} = r_{l,g''} = 0$) as it is considered in this paper, the three sequent parts $S_{g'}$, S_l, and $S_{g''}$ of the ECDL can be treated as a single *gap* section S_g with the averaged group index $\langle n_g\rangle_g$, phase tuning $\langle\delta\rangle_g$, and loss $\langle\alpha\rangle_g$. Here, $\langle\zeta\rangle_k = \frac{1}{|S_k|}\int_{S_k}\zeta(z)dz$ denotes a spatial average of a function ζ over any ECDL section S_k, whereas $|S_k|$ is the length of S_k. The TW equations (1) in S_g can be easily resolved implying

$$E^+(z_{g'',b}^-,t) = \sqrt{\eta}e^{i\varphi/2}E^+(z_{a,g'}^+,t-\tau_g), \qquad E^-(z_{a,g'}^+,t) = \sqrt{\eta}e^{i\varphi/2}E^-(z_{g'',b}^-,t-\tau_g),$$

where

$$\eta = e^{-\langle\alpha\rangle_g|S_g|}, \;\; \frac{\varphi}{2} = -\langle\delta\rangle_g|S_g|, \;\; \text{and} \;\; \tau_k = \frac{\langle n_g\rangle_k|S_k|}{c_0}$$

are the intensity attenuation, the phase shift of the forward or backward field during its propagation along S_g, and the field propagation time along each ECDL part S_k, respectively.

Within the active section S_a, the remaining terms of the propagation factor β are nontrivial. The operator $\mathcal{D}$ together with the induced polarization functions $P^{\pm}(z,t)$ are used to model the dispersion of material gain by a Lorentzian approximation [8]:

$$\mathcal{D}E^{\pm} = \overline{g}(E^{\pm} - P^{\pm}), \qquad \partial_t P^{\pm} = \overline{\gamma}(E^{\pm} - P^{\pm}) + i\overline{\omega}P^{\pm}, \tag{4}$$

where $\overline{g}$, $\overline{\omega}$, $2\overline{\gamma}$ are the amplitude, the relative central frequency, and the full width at the half maximum of this Lorentzian. The function $\delta_T(I) = c_T I$ represents the dependence of the refractive index on the heating induced by the injected current I [12]. The thermal tuning factor $c_T \approx \pi/(|S_a|\Delta_I)$ implies the experimentally observed mode jumps with a change of the injected current [9, 12]. The value $c_T = 1.366\cdot 10^5\ \mathrm{A^{-1}m^{-1}}$ used in our case corresponds to an

average spacing between the mode jumps of $\Delta_I \approx 23$ mA and is in a good agreement with a similar parameter used in [12].

The factor β depends also on the carrier density dependent gain and index change functions determined by the confinement factor Γ, differential gain g', linewidth enhancement (Henry) factor α_H, and transparency carrier density N_{tr}. Due to the fact, that in the ECDL under study the overall variation of the carrier density N is small, a linear dependence on N has been assumed [13].

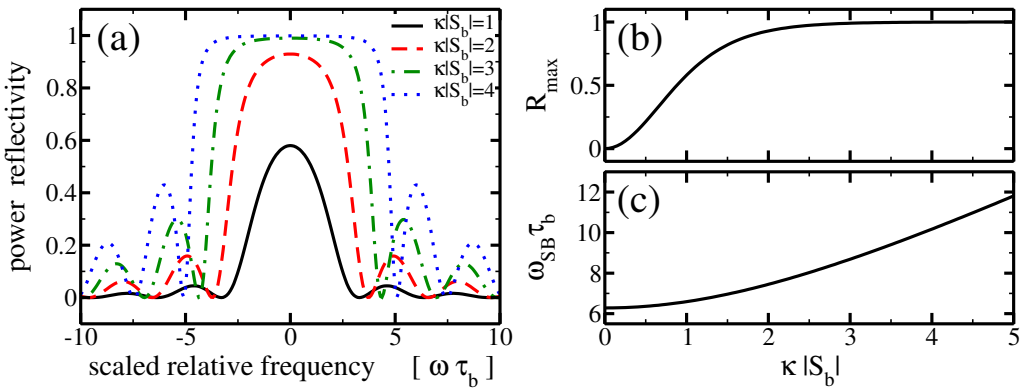

Figure 2: Reflectivity spectra of the BG for several values of $\kappa|S_b|$ (a). The dependence of the peak reflectivity (b) and stop-band width (c) on $\kappa|S_b|$.

The field coupling coefficient factor κ in Eqs. 1 is non-vanishing only in the Bragg grating section S_b. Fig. 2(a) shows spectra of the intensity reflection for different values of $\kappa|S_b|$ and for vanishing α and δ within S_b and vanishing reflection r_L at $z = L$. The maximal field intensity reflection $R_{max} = \tanh^2(\kappa|S_b|)$ (achieved for the relative frequency $\omega_{max} = -\delta c_0/n_g$) and the stop band width $\omega_{SB} = \frac{2}{\tau_b}\sqrt{\kappa^2|S_b|^2 + \pi^2}$ (measured as the separation of the closest local minima at the both sides of the stop band) are uniquely determined by the scaled coupling $\kappa|S_b|$ (see Fig. 2(b) and (c)). In the considered case, for $|S_b| = 6$ mm and $R_{max} = 0.7$, the coupling coefficient $\kappa \approx 2.017$ cm^{-1} and the stopband width (measured as a separation of the adjacent to the stop band local minima of the reflectivity spectrum) $\omega_{SB}/2\pi \approx 36$ GHz.

The longitudinal distribution of the local photon density $|E(z,t)|^2 = |E^+|^2 + |E^-|^2$ within the active section S_a of the ECDL deviates only slightly from its spatial average, $\langle|E|^2\rangle_a$. For this reason we neglect the spatial hole-burning of carriers and define the evolution of the spatially-uniform carrier density $N(t)$ in the active section S_a by the following rate equation:

$$\partial_t N = \frac{I}{q\sigma|S_a|} - \left(AN + BN^2 + CN^3\right) - \frac{c_0}{n_g}\Re\sum_{\nu=\pm}\langle E^{\nu *}\left[\Gamma g'(N-N_{tr}) - \mathcal{D}\right]E^{\nu}\rangle_a, \quad (5)$$

where A, B, C are carrier recombination parameters, I, σ, and q denote the injected current, the cross-section area of the active zone, and the electron charge.

The ECDL operates at $\lambda_0 = 0.78\mu$m. The amplitude reflectivities $r_{g',l} = r_{l,g''} = 0$. Other reflectivities are $r_{a,g'} = 0.01$, $r_{g'',b} = r_L = 0$, and $r_0 = \sqrt{0.3}$. The typical lengths of sections are $|S_a| = 1$ mm, $|S_b| = 6$ mm, and $|S_g| = 30$ mm (where $|S_{g'}|$, $|S_l|$, and $|S_{g''}|$ are 1,

2, and 27 mm, respectively). The group indices n_g in S_a, S_b, S_l, and $S_{g',g''}$ are 4.1, 1.48625, 1.6005, and 1, respectively. For more details and typical values of all other parameters, see Refs. [14, 13].

2.2 Coexistence of multiple stable steady states

It is well known that an analysis of optical modes of the model equations (1–5) can provide a deep understanding of different dynamic effects in various multi-section semiconductor lasers and, particularly, in ECDL devices, see Refs. [9, 10, 11, 14] for more details. Instantaneous optical modes are sets of complex-valued objects $(\Theta(z), \Omega)$, which satisfy the spectral problem generated by the substitution of the expression $E(z,t) = \Theta(z)e^{i\Omega t}$ into the field equations (1), (2), and (4). Both $\Theta(z)$ and Ω depend on the instantaneous value of carrier density $N(t) = \bar{N}$. The real and imaginary parts of the complex eigenvalue Ω of the spectral problem represent the optical frequency and the damping of the mode, respectively. The vector-eigenfunction $\Theta(z)$ gives us the spatial profile of the longitudinal mode [10].

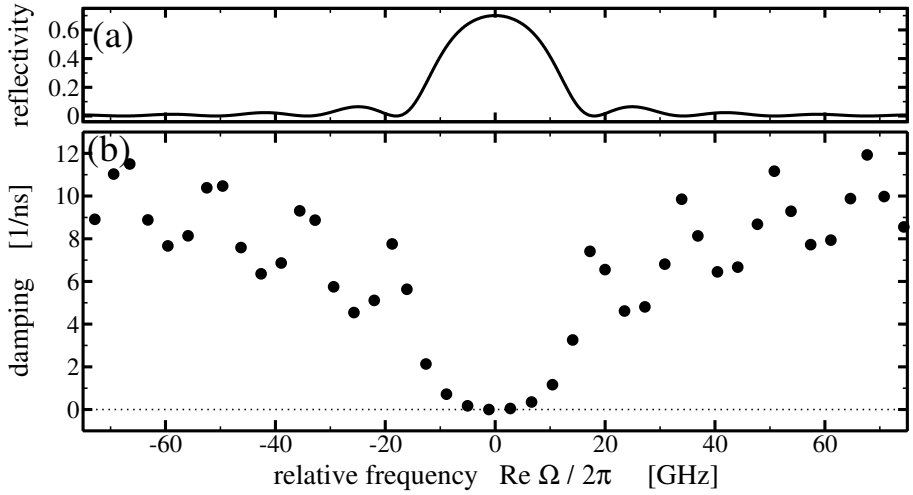

Figure 3: Reflectivity spectra of the BG (a) and complex frequencies Ω of the most important instantaneous modes (b) computed for $\bar{N} \approx 1.77 \cdot 10^{24}$ m^{-3}, which was obtained after the long transient integration of the TW model (1–5) for $I = 80$ mA.

A typical example showing the most important mode frequencies Ω of the ECDL is given in Fig. 3(b). Note, that 5 modes located within the stop-band of the BG [see Fig. 3(a)] have rather small damping, which does not exceed $1\,\text{ns}^{-1}$. Thus, a strong influence of the side modes still can be expected, even though the ECDL operates at a cw state determined by one of these modes.

All stationary (continuous wave) states of the TW model (1–5) can be written as

$$(E(z,t), N(t)) = \left(\Theta(z)e^{i\omega t}, \bar{N}\right), \tag{6}$$

where $(\Theta(z), \omega)$ is an instantaneous optical mode computed at the mode *threshold* carrier density $\bar{N}$, which provides the *real*-valued mode frequency ω, i.e., determines the mode with

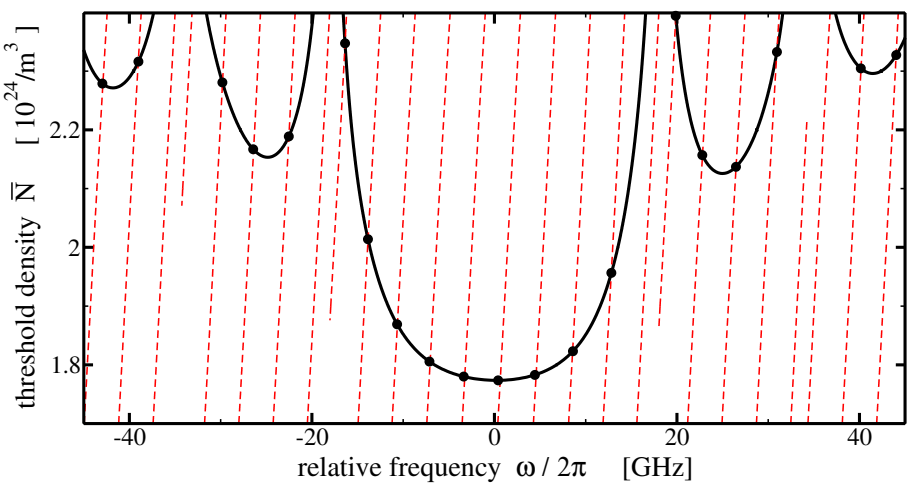

Figure 4: Representation of cw states in mode frequency ω - mode threshold $\bar{N}$ domain. Solid: cw states for fixed $\eta = 0.8$. Dashed: cw states for fixed $\varphi = 0$. Bullets: cw states for fixed φ and η.

no damping or amplification. Thus, in order to find all possible cw states we need to find all real pairs $(\bar{N}, \omega)$ solving the spectral problem [10]. Some of such pairs with smallest threshold densities $\bar{N}$ are indicated by black bullets in Fig. 4. These bullets are at the intersection of the solid and dashed curves, which represent all possible steady states for fixed η but arbitrary φ and fixed φ but arbitrary η, respectively. For more details, see Ref. [14].

The phase factor φ can be used for parameterization of the solid fixed-attenuation curves in Fig. 4, what allows a standard representation of the steady state branches. Thin solid curves in panels (a) and (b) of Fig. 5 show these parametric representations of $\omega = \omega(\varphi)$ and $\bar{N} = \bar{N}(\varphi)$, respectively. Due to the periodicity of factor φ, all these curves can be re-obtained after a 2π-shift along the abscissa axis. This periodicity implies the coexistence of multiple cw states for each fixed phase. For example, there are four states with $\bar{N} < 1.81 \cdot 10^{24}\,\mathrm{m}^{-3}$ for $\varphi = 0$ (see number of solid lines at this phase in Fig. 5(b) and number of bullets for those threshold densities in Fig. 4).

The mode analysis and the semi-analytic location of the steady states, however, do not provide any information about the stability of these states. In general, a detailed investigation of the stability of the states can be performed by means of numerical bifurcation analysis [11]. In our case, however, the stability of each cw state is identified by its ability to attract trajectories during numerical integration of the model equations. For this reason, we perform large transient simulations of the TW model (1–5) and determine the side-mode suppression ratio μ_1 in the optical spectra (Fourier-transformed complex optical field $E^-(0,t)$ at the left facet of the ECDL) and the relative deviation $\mu_2 = \frac{\max_t P_o - \min_t P_o}{\max_t P_o + \min_t P_o}$ of the emitted field intensity $P_o(t)$. The states characterized by $\mu_1 > 20\,\mathrm{dB}$ and $\mu_2 < 0.02$ obtained during numerical integration of the TW model with step-wise increasing or decreasing φ are represented by large red and small blue bullets in Fig. 5. One can see, that the location of these numerically observed states coincide with some of our semi-analytically obtained steady state branches.

It is noteworthy, that except for the tiny regions close to the observed transitions between the

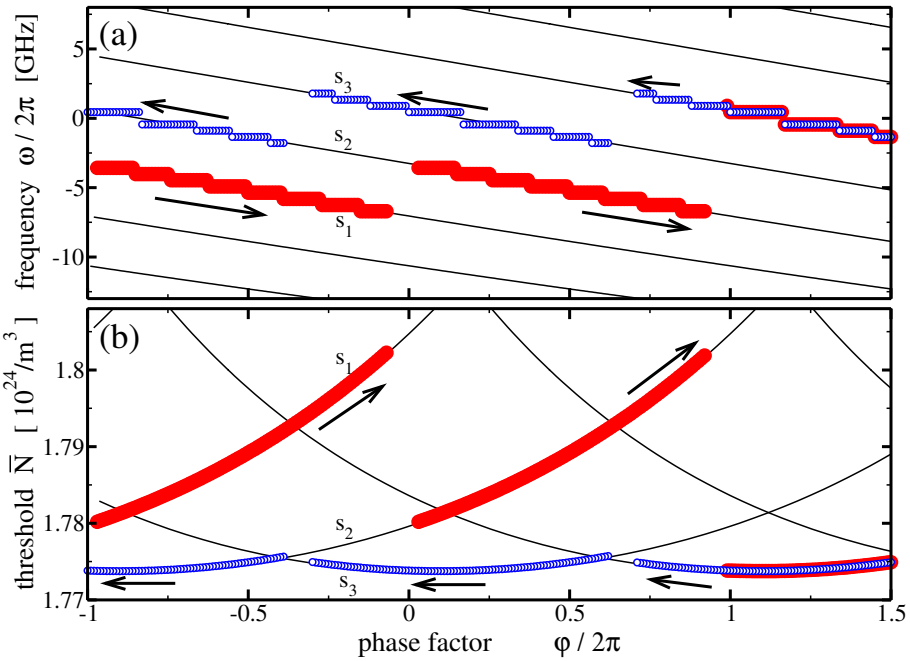

Figure 5: Frequencies ω (a) and thresholds $\bar{N}$ (b) of steady states as functions of φ for $I = 60\,\mathrm{mA}$. Thin solid curves: semi-analytically located states for fixed $\eta = 0.8$. Large red (small blue) bullets: stable states obtained by model integration with increased (decreased) φ. Parameters as in Fig. 4.

different states, the simulations show a stable cw emission. For decreased φ, the cw state is defined by the maximal gain (minimal threshold) mode. Once the threshold $\bar{N}$ of the adjacent mode approaches the threshold of the operating mode (close to $\varphi/2\pi = -0.35$ or 0.65), the switching to this side mode takes place. For increased φ, the situation is different. In most cases, the operating cw state is different from the maximal gain mode. Just before the state switches (at phases $\varphi/2\pi \approx 0$ or 1) the operating cw state is defined by the mode with the fourth smallest threshold. Moreover, the state transitions after the loss of stability in this case lead to different cw states. This is a manifestation of the multi-stability in the ECDL devices.

Three different stable cw states were found for $\varphi/2\pi = -0.2$. The thresholds and the frequencies of these states, denoted as s_i, $i = 1, 2, 3$, are shown in Fig. 5, whereas the optical spectra and the emitted power of the field at both sides of the ECDL are represented in Fig. 6. It is not very surprising, that the smallest-threshold state s_3 has the largest emission at the active-section side of the ECDL (see Fig. 6(c)). Comparing to the other states, a smaller part of the injected current in this case is used to keep the carrier density at threshold, whereas the remaining larger part implies the larger emission. Probably, a bit unexpected is the large emission at the BG side shown by the largest-threshold state s_1 (see Fig. 6(d)). The wavelength of the state s_1, however, is more dislocated from the middle of the stop-band. Thus, the cw state s_1 gets a smaller reflection from the BG (what increases the mode threshold), but also has a larger transmission through the grating, which results in a larger emission of the field (see Fig. 6(a,b)).

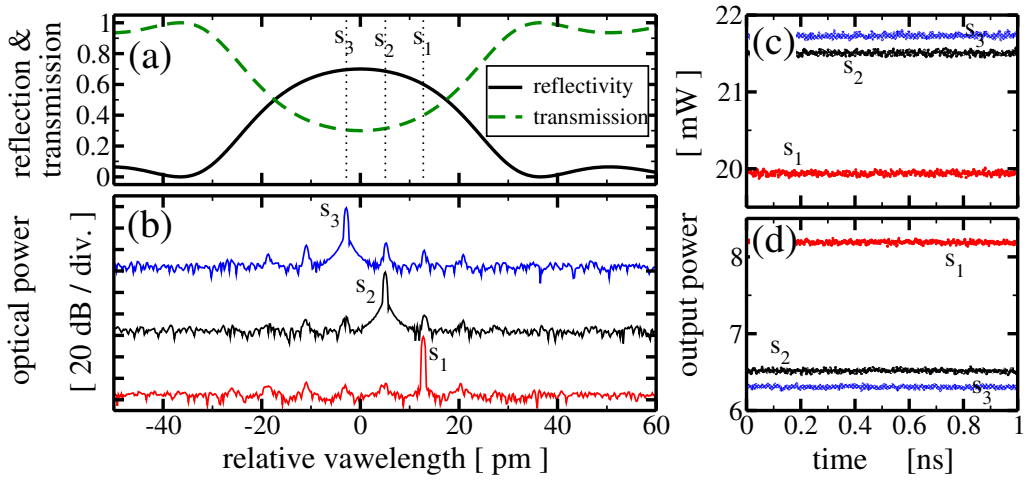

Figure 6: Simulated reflectivity and transmission spectra of the BG (a), optical spectra (b) and the emitted field power at the active-section (c) and BG (d) sides of the ECDL of three different stable cw states for $\varphi/2\pi = -0.2$. Other parameters as in Fig. 5.

2.3 Experiments vs. numerical simulations

To validate the simulation results a micro-integrated ECDL was investigated experimentally at FBH Berlin. A comparison of the measurements and simulations is performed in Fig. 7. Panels (a) and (c) of this figure represent typical experimentally observed state-exchange behavior in ECDL devices for increased and decreased injection currents induced by thermal detuning [9, 12, 13, 14]. First of all, this figure confirms a theoretically predicted coexistence of the multiple stable steady states, which can be accessed by changing the direction of the current sweep. The wavelengths of two different lasing states for $I \approx 125$ and 150 mA are separated by, approximately, 8.63 pm, which corresponds to the separation of the neighboring optical modes within the stop-band of the BG. The two times larger wavelength separation for $I \approx 140$ and between 155 and 186 mA indicates a possible coexistence of the third stable state, which could be accessed by a change of the direction of the current sweep just after each jump of the states.

The similar simulated state-jumping behavior is represented in panels (b) and (d) of the same figure. In order to obtain the good agreement between measurement and simulation, the maximum reflectivity of the BG has to been changed from the intended value $R_{max} = 0.7$ to $R_{max} = 0.5$ by a corresponding adaptation of the coupling coefficient κ. The reasons for this adjustment could be, for example, the divergence of the beam within the BG and an imperfect alignment of the BG with respect to the optical axis of the ECDL.

It is noteworthy, that the states observed during the down-sweeping of the injection current have larger intensities, as compared to the up-sweeping case. The wavelengths of these states are located close to the center of the BG stop-band, which in our simulations is at 780 nm. Small differences of the emitted field intensities before and after mode jumps in this case can be well explained by the similar emission power of the states s_3 and s_2, see Fig. 6(c). On contrary, the state jumps for up-swept injection correspond to detuning induced transitions between states

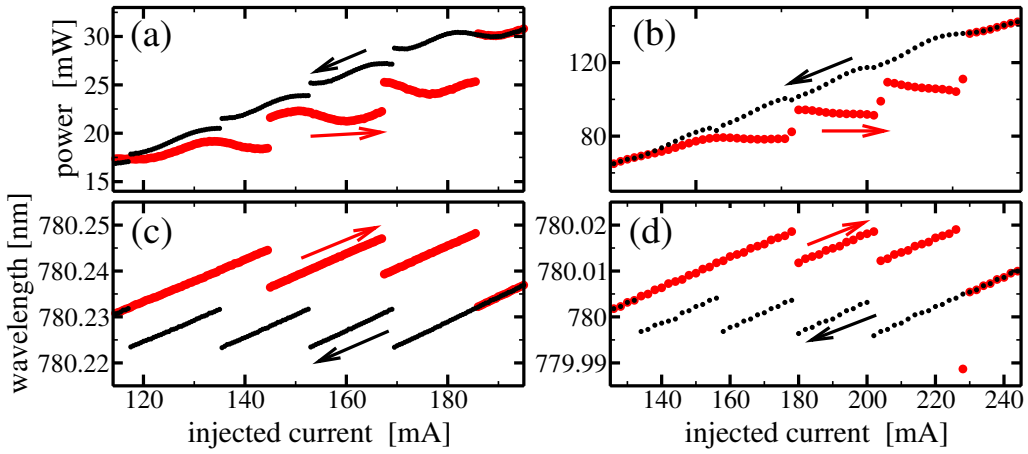

Figure 7: The mean output power at the left facet of the ECDL (a,b) and the dominant lasing wavelengths (c,d), as functions of the increased (red) or decreased (black) injected current in experiments (left) and simulations (right). In simulations, $R_{max} = 0.5$, whereas all other parameters are as in the examples before.

s_1 and s_2 or s_1 and s_3 (see Figs. 5 and 6), what explains the large step-like increase of the emission intensity at each state transition.

2.4 Parameter study

As it was mentioned above, the dynamics of the ECDL device is determined by several modes in many cases. In order to achieve a controllable stable lasing on a single mode, one needs to improve the mode selection, which, particularly, can be achieved by a reduction of the number of the main modes almost equally supported by the BG.

First of all, we consider the device with the BG peak reflectivity $R_{max} = 0.7$. A detailed analysis of this ECDL device for increased and decreased injection current over larger injection range is presented in Fig. 8. The problem of frequently occurring multi-mode non-stationary states is well illustrated by panels (a) and (c) of this figure. Hatched regions in panel (a) indicate the existence of the non-stationary states with relative deviation factor $\mu_2 > 0.02$. In panel (c), small black and red dots showing the positions of side peaks with $\mu_1 < 20$ dB in optical spectra coincide with the wavelengths of the semi-analytically computed modes (thin grey-dotted lines). Thus, the dynamic states in these regions are determined by a beating between similarly damped longitudinal modes located within the stop-band of the BG. It is noteworthy, that for larger injection currents, $I > 150$ mA, up to five different modes can significantly contribute to the dynamic states (see multiple large and small bullets in Fig. 8(c) at these injection currents). At the same time, for smaller injection currents, $I < 100$ mA, only two or three modes can be excited, implying a more stable stationary operation of the device.

Increasing the injection current allows the achievement of stationary and non-stationary states with an (averaged) carrier density, that is significantly exceeding the density $\bar{N}$ of the minimal threshold mode (compare red and black curves in Fig. 8(b)). For the up-sweep bias current,

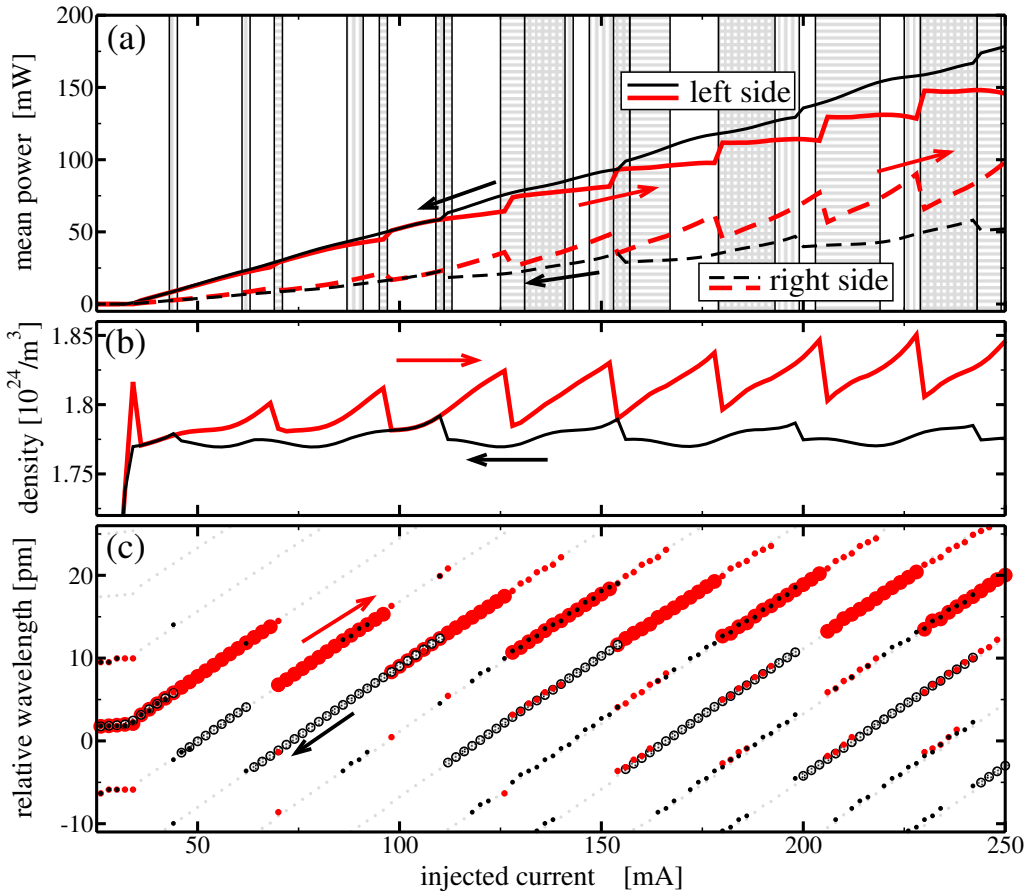

Figure 8: Mean output power at both sides of the ECDL (a), mean carrier density in S_a (b), and lasing wavelengths (c) as functions of increased (red) or decreased (black) pumping. Horizontally (vertically) hatched areas in (a): non-stationary regimes for increased (decreased) pumping. Big bullets and small dots in (c): main optical mode and side modes suppressed by less than 20 dB. Thin dashed grey lines: longitudinal mode positions.

typical transitions between the states are characterized by the jumps to the shorter lasing wavelength located closer to the central wavelength of the BG [red bullets in panel (c)], sudden reduction of the mean carrier density [panel (b)] and increase (decrease) of the (mean) emission intensity at the left (right) output port of the ECDL [panel (a)]. The lasing wavelength and emission intensities before and after the transitions are similar to those of the states s_1 and s_2 shown in Fig. 6. A corresponding transition from s_1 to s_2 was also shown in Fig. 5 at the phase $\varphi \approx 0$. The jumps of the carrier density and emission intensities for decreased injection current are less pronounced, since the dominant mode wavelengths are closer to the middle of the stop-band and their thresholds are rather similar.

In what follows, we have repeated simulations of Fig. 8 using smaller κ and, therefore smaller reflectivity of the BG, $R_{max} = 0.4$. As it can be seen from Fig. 9 (a) and (c), the reduction of κ implies a reduction of the emission intensity at the left side of the ECDL, and, which is rather important, stabilizes the laser operation between the mode transitions. The gratings with large $\kappa|S_b| \geq 2$ have a flat stop-band [see Fig. 2(a)], which can equally support multiple modes

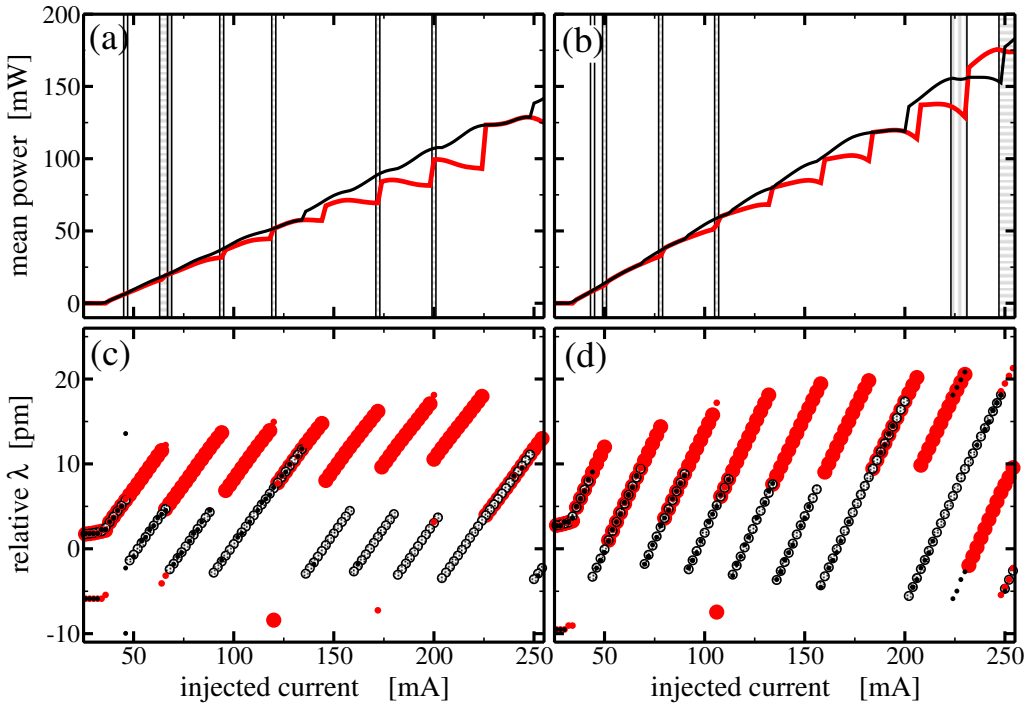

Figure 9: Mean left facet output power (top) and the lasing wavelengths (bottom) as functions of the increased (red) or decreased (black) pumping. Left: peak reflectivity $R_{max} = 0.4$, air gap length $|S_{g''}| = 27$ mm. Right: $R_{max} = 0.7$, $|S_{g''}| = 13$ mm. All other parameters are as in Fig. 8.

(once they are located within such a stop-band). Thus, even though the choice of a smaller $\kappa|S_b| \approx 0.75$ [see Fig. 2(b)] reduces the overall reflectivity of the grating and implies an unwanted increase of the lasing threshold as well as decrease of the emission intensity, it helps to improve the side mode suppression.

Another way to achieve effective control of the modes is provided by a reduction of the air gap length, i.e., an increase of the mode separation and, therefore, the reduction of the number of modes supported by the BG. Panels (b) and (d) of Fig. 9 give an illustration of the simulated dynamics in the shortened ECDL with $|S_{g''}| = 13$ mm (compare it to $|S_{g''}| = 27$ mm used in the previous examples). It is noteworthy, that the stabilization of the ECDL in this case is achieved without the reduction of the emission power.

A set of simulations of the ECDL devices with varying R_{max} and $|S_g|$ for different values of the injected current are summarized in panels (a) and (b) of Fig. 10. Here we show the number of stable coexisting cw states in different parameter domains in the absence of non-stationary attractors. White areas in these diagrams show the regimes were the ECDL is below threshold or posses at least one stable non-stationary regime. Yellow, red, and black colors indicate the parameters where a single, two or three different stable cw states could be observed. To access numerically each of these states, we have applied 10 ns long optical pulse injections with the optical frequencies determined by each of the six modes located within the stop-band of the BG (see Fig. 3). The presence of the stable cw state was decided after 100 ns transients using the

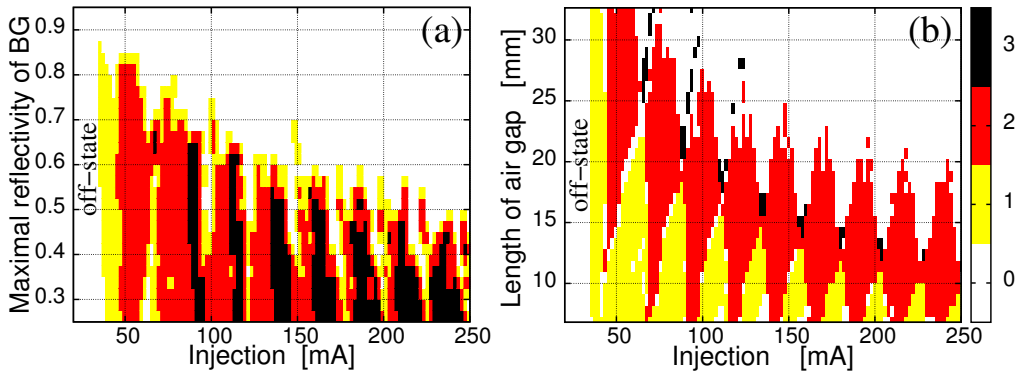

Figure 10: Number of stable cw states in ECDL devices for different values of injection current and tuned κ in the BG but fixed length $|S_g|$ (a) and tuned length $|S_g|$ but fixed κ in the BG (b). All other parameters are as in the examples before.

spectral and temporal criteria $\mu_1 > 20$ dB, $\mu_2 < 0.02$, as discussed in Section 2.2. Note also, that horizontal sections of diagram (a) at $R_{max} = 0.4$ and of diagram (b) at $|S_g| = 16$ mm correspond to the two situations considered in Fig. 9.

The white color regions at the upper right part of these diagrams confirm the occurrence of the mode beating solutions for high injection current and high R_{max} or long $|S_g|$. Thus, in order to manufacture devices with suppressed mode-beating dynamics within a large injected current range, one should use a moderate peak reflectivity of the BG and / or reduce the air gap length. The reduction of the air gap also implies a broadening of the injected current regions where the only lasing state is a continuous wave state: see yellow color regions at the lower part of Fig. 10(b).

3 Delay differential equation model

To make the investigations of the ECDL devices easier, it is preferable to have some easier models admitting different analytic and semi-analytic methods of their analysis. In this section we discuss two possible modeling approaches based on delay differential equations (DDEs) [15]. The first of these approaches is a well-known DDE model of Lang-Kobayashi (LK) type, which was originally used for the investigation of the dynamics in single-mode lasers with *long* ECs and *weak* optical feedback [4]. The second approach is a newly derived multi-mode (MM) DDE model suited for simulations of the Fabry-Perot type diode laser with an optical feedback from the external cavity (EC), see Fig. 11(a). To demonstrate advantages of this new model, we compare it to properly normalized TW and LK models.

External cavity. In all three cases, we assume that the action of the EC, i.e., the relation between the optical field $F_i(t)$ re-injected into the diode and the field $F_e(t)$ emitted from the diode is given by the linear operator $\mathcal{F}$. For the simple EC determined by an external mirror, $\mathcal{F}$ is, basically, a simple time-delay operator:

$$F_i(t) = [\mathcal{F}F_e](t) = Ke^{i\phi}F_e(t-\tau), \tag{7}$$

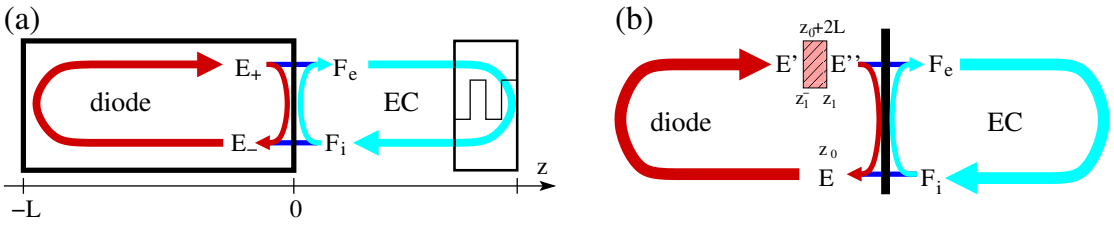

Figure 11: Schematic representations of the diode laser with an external cavity. (a): linear configuration, as considered in the TW model. (b): ring diode laser configuration (left) with a localized filtering element (hatched box) and the filtered optical feedback from the external cavity (right), as considered in the new MMDDE model.

where τ is the field round-trip time in the EC, whereas K and ϕ are the transmission factor and the phase shift of the complex field amplitude during this round-trip. More sophisticated ECs can contain several reflectors or different frequency filtering elements, such as passive resonators or Bragg gratings. The action of various objects of the EC can be approximated by linear continuous time filters described by ODEs. For example, the delay operator (7) can be interpreted as a broad Lorentzian filter,

$$\begin{array}{l} F_i(t) = [\mathcal{F}F_e](t) = \tilde{\gamma} K e^{i\phi} \int_{-\infty}^{t-\tau} e^{-\tilde{\gamma}(t-\tau-\nu)} F_e(\nu) d\nu \qquad \Rightarrow \\ \frac{1}{\tilde{\gamma}} \frac{d}{dt} F_i(t) = K e^{i\phi} F_e(t-\tau) - F_i(t), \end{array} \tag{8}$$

in the limit case of $\tilde{\gamma} \to +\infty$. For the sake of simplicity, we consider only the simplest case of the EC determined by Eq. (7) or Eq. (8). We note, however, that the EC typical for ECDL devices can be easily modeled by the same Eq. (8) with a finite parameter $\tilde{\gamma}$, or by some other nonlocal operator $\mathcal{F}$ admitting its replacement by a single or a few differential equations.

Traveling wave model. After a suitable normalization [16], the spatially-distributed TW model within the laser diode can be written as

$$\begin{array}{c} (\partial_t \pm \partial_z) E_\pm = \left((1+i\alpha_H) n - \frac{\xi_0}{L} - \mathcal{P} \right) E_\pm, \\ \mathcal{P} E_\pm = \frac{\bar{g}}{2} \left(E_\pm - P_\pm \right), \ \frac{d}{dt} P_\pm = \bar{\gamma} E_\pm + (i\bar{\omega} - \bar{\gamma}) P_\pm, \\ \epsilon^{-1} \frac{d}{dt} n = J - n - \Re \left\langle (E, [2n + 1 - 2\mathcal{P}] E) \right\rangle, \\ E_+(-L,t) = -r_f^* E_-(-L,t), \ \begin{pmatrix} F_e(t) \\ E_-(0,t) \end{pmatrix} = \begin{pmatrix} t_r & -r_r^* \\ r_r & t_r \end{pmatrix} \begin{pmatrix} E_+(0,t) \\ F_i(t) \end{pmatrix}. \end{array} \tag{9}$$

Here, $E = (E_+, E_-)^T$, $(\cdot,\cdot)$ and $\langle \cdot \rangle$ are scalar product of vector functions and spatial average, respectively. The complex factor ξ_0 is determined by the relation $e^{2\xi_0} = -r_f^* r_r e^{-2\chi(0)}$, where r_f and r_r are complex field amplitude reflection coefficients at the the front ($z = -L$) and rear ($z = 0$) diode facets, $\chi(\omega) = \frac{\bar{g}L}{2} \frac{i(\omega-\bar{\omega})}{\bar{\gamma}+i(\omega-\bar{\omega})}$, $t_r = \sqrt{1-|r_r|^2}$, whereas F_e and F_i are related by Eq. (7).

Lang-Kobayashi type model. The normalized LK type model can be written as

$$\begin{array}{l} \frac{d}{dt} E = (1+i\alpha_H) n E + C F_i, \ \ F_i(t) = [\mathcal{F}E](t), \\ \epsilon^{-1} \frac{d}{dt} n = J - n - (2n+1)|E|^2, \end{array} \tag{10}$$

where the operator $\mathcal{F}$ and parameters J, ϵ and α_H are the same as in the TW model discussed above. The coefficient $C = \frac{t_r^2}{2r_r L}$ relates the feedback *rate* (which in non-scaled LK model would have the dimension s^{-1}) with the dimensionless field transmission factor $Ke^{i\phi}$ from (7) [16].

Multi-mode DDE model. Following Ref. [17], we neglect the back propagating field E_- in the TW model, assume the ring configuration of the diode laser, and allow the spatial distribution of carriers. We assume that all distributed field amplitude losses, frequency detuning, and field dispersion within the diode are concentrated within a single point source [hatched box in Fig. 11(b)], whereas the relation of the incident and transmitted fields $E'(t)$ and $E''(t)$ [see notations in Fig. 11(b)] are defined by

$$\frac{d}{dt}E''(t) = (\gamma' - i\bar{\omega})\left(\mu E'(t-\Delta) - E''(t)\right), \qquad \text{where}$$
$$\gamma' = \frac{\bar{\gamma}}{\sqrt{2\bar{g}L}}, \;\; \mu = \frac{e^{-(1+i\alpha_H)L}}{r_r}, \;\; \Delta = \frac{\bar{g}L - \sqrt{2\bar{g}L}}{\bar{\gamma}} = \tau_d - 2L.$$

After resolving the unidirectional TW equation, introducing forward along the characteristic line performed sliding average of the carrier densities, $\tilde{n}(t) = \frac{1}{2L}\int_{z_0}^{z_1} n\left(\nu, t+\nu-z_0\right) d\nu$, eliminating E', E'', F_e, and introducing a new function $F = \frac{1}{t_r}F_i$, we obtain the following MMDDE model for lasers with an external feedback:

$$\begin{aligned}
\frac{d}{dt}E &= -[\gamma' - i\bar{\omega}]E(t) + t_r^2\left[\gamma' - i\bar{\omega} - \tilde{\gamma}\right]F(t) + t_r^2\frac{\tilde{\gamma}Ke^{i\phi}}{r_r}\left[E(t-\tau) - F(t-\tau)\right] \\
&\quad + (\gamma' - i\bar{\omega})e^{(1+i\alpha_H)\tilde{n}(t-\tau_d)2L}E(t-\tau_d), \\
\frac{d}{dt}F &= -\tilde{\gamma}F(t) + \frac{\tilde{\gamma}Ke^{i\phi}}{r_r}\left[E(t-\tau) - F(t-\tau)\right], \\
\epsilon^{-1}\frac{d}{dt}\tilde{n} &= J - \tilde{n} - \frac{1}{2L}\left[e^{[2\tilde{n}+1]2L} - 1\right]|E|^2 .
\end{aligned} \tag{11}$$

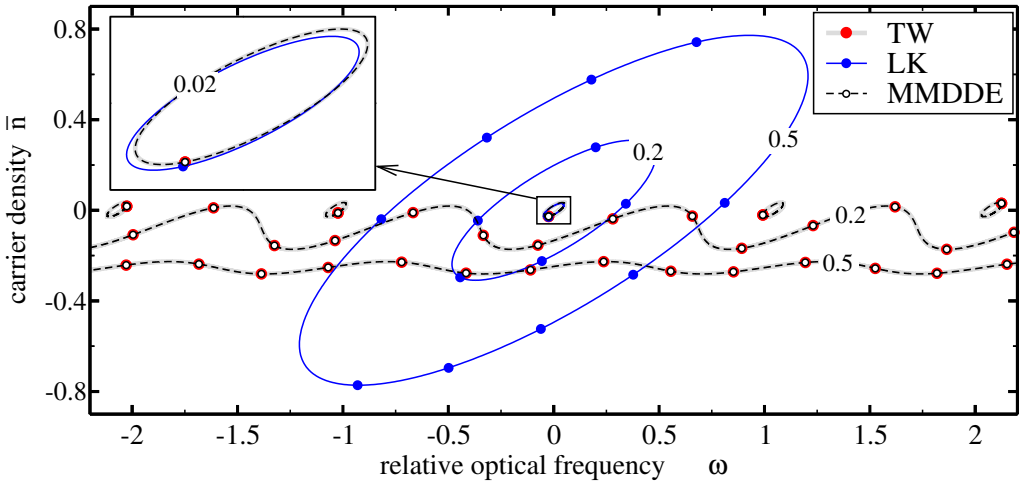

Figure 12: Curves of CMs in the TW (thick grey), LK (thin solid) and MMDDE (thin dashed) models for arbitrary ϕ and $K = 0.02$, $K = 0.2$, and $K = 0.5$, whereas $L = 3$, $\tau = 13.5$, $\alpha_H = 1.2$, $r_f = \sqrt{0.3}$, $r_r = e^{-2.84}/r_f \approx 0.1$, $\bar{\omega} = 0$, $\bar{g} = 6$, $\bar{\gamma} = 120$, $\tilde{\gamma} = 500$. Bullets on the corresponding curves show location of the cavity modes for fixed $\phi = 0$. An insert shows enlarged curves for $K = 0.02$ in the vicinity of origin, $(\omega, \bar{n}) = (0, 0)$.

Comparison of models. Cavity modes (CMs), which are the steady states of the corresponding system, can be defined by the threshold carrier density $\bar{n}$ and the relative optical frequency ω.

The choice of the scaling factor C in the LK model [16] and the parameters γ', μ, Δ in the MMDDE model allow to get a best fitting of the CMs in the reduced DDE models to the CMs of the TW model.

Different curves in Fig. 12 represent all possible locations of the CMs for fixed feedback amplitude factor K and arbitrary feedback phase ϕ. It can be clearly seen, that for small K, the CMs of the LK model provide a good approximation of the CMs of the TW model in the vicinity of the origin $(\omega, \bar{n}) = (0, 0)$, see thin blue and thick grey solid curves within the insert of Fig. 12. We note, however, that for small K and fixed φ, the LK modes has a unique CM (blue diamond in Fig. 12), whereas the TW model posses multiple CMs with similar separation ($\sim \pi/L$) of mode frequencies ω and similar thresholds $\bar{n}$ (red bullets in Fig. 12). For moderate and large K, the agreement between LK and TW equations is drastically degraded: whereas CMs of the LK model are located on the increasing ellipses centered around the origin $(0, 0)$, the CMs of the TW model are on a single, only slightly undulated nearly horizontal non-connected curve. In contrast, the CMs of our new MMDDE model are in nearly perfect agreement with the CMs of the TW model for all values of K: see indistinguishable thin dashed and thick grey curves in Fig. 12.

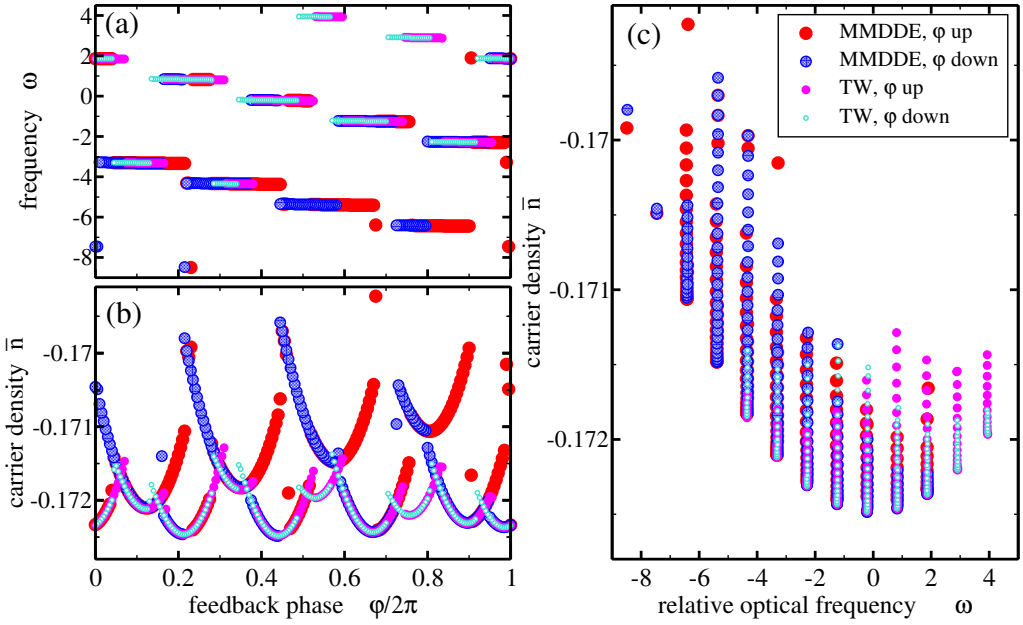

Figure 13: Changes of states during numerical integration of the TW and MMDDE with increased and decreased φ. (a) and (b): main frequency and mean carrier density as functions of φ. (c): same calculations in frequency-density plane. $K = 0.2$, $J = 2$, $\epsilon = 4 \cdot 10^{-3}$, whereas other parameters as in Fig. 12.

Another comparison of the MMDDE and TW models is presented in Fig. 13. Here, we have performed an estimation of the states for different values of the feedback phase factor ϕ using direct numerical integration of two different models. Panels (a) and (b) of this figure show the observed multiple transitions between different CMs. All observed states are also indicated by different bullets in the frequency-carrier density plane (panel (c) of the same figure). It is noteworthy that all these states represent only those CMs which are located close to the multiple-minima of the

thick solid and thin dashed curves corresponding to the case $K = 0.2$ in Fig. 12. The frequency separation of these states is, approximately, π/L, what corresponds to the separation of the FP laser resonances.

Conclusions. In conclusion, we have shown that our new MMDDE model is able to reproduce the basic features of the TW model for the FP-type lasers with external feedback, whereas LK-type models are giving a satisfactory agreement only in the case of weak feedback. Due to large feedback in the ECDL devices, one should better use our MMDDE model instead of the LK model.

4 New user interface of the software LDSL-tool

LDSL-tool is a software for simulation and analysis of the (L)ongitudinal (D)ynamics in multi-section (S)emiconductor (L)asers. This software is based on Traveling Wave (PDE) equations describing the propagation of optical fields along the longitudinal direction of the laser. The field equations are nonlinearly coupled with the ordinary differential equations for carrier densities and polarization functions. LDSL-tool not only integrates the PDE model equations but also allows to analyze the dynamics of longitudinal modes and to build reduced ODE models based on a finite number of modes. After showing good qualitative and quantitative agreement between Traveling Wave and Mode Approximation models, the reduced models can be analyzed with common tools for bifurcation analysis such as AUTO. Such different possibilities together with some data post-processing routines make our software a powerful tool suited for simulation and analysis of various dynamical effects in semiconductor lasers.

The kernel of LDSL-tool is a C++ code which integrates model equations, calculates instantaneous optical modes and performs a field expansion into modal components. Before this project, the user interface of LDSL-tool was created using RLaB, which is a free available interactive, interpreted scientific programming environment. Some RLaB routines (~ 15.000 lines of RLaB code) are used for loop computations, parameter optimization, analysis, representation (plotting), post-processing, and evaluation of different criteria of the computed data. These routines allow an automatic extraction of some main features of the computed solutions (e.g., the peak magnitudes and frequencies in radio-frequency or optical spectra, the maxima, minima or mean values of field intensity, the width and jitter of pulsations, etc.). These few characteristics are collected when running automatic computations and looking for the device performance in different parameter domains.

An advantage of RLaB is that it is an open source programming language. Disadvantages are i) the lack of support and ii) it is not known for the majority of possible users of LDSL-tool. It is noteworthy that RLaB is a programming language similar to MATLAB but with some features that remind of C++. That means that most functions and structures can be translated one to one. The main differences lie in the naming of structures and fields, the definition of local and global variables and the saving and reading of files. A significant difference exists as well in the plotting of data. Seeking to make our software better available for a larger community, we have decided to translate the RLaB-based user interface to a MATLAB-based one. This task was mainly performed by the student research assistant Mara Oßwald, who in a rather limited

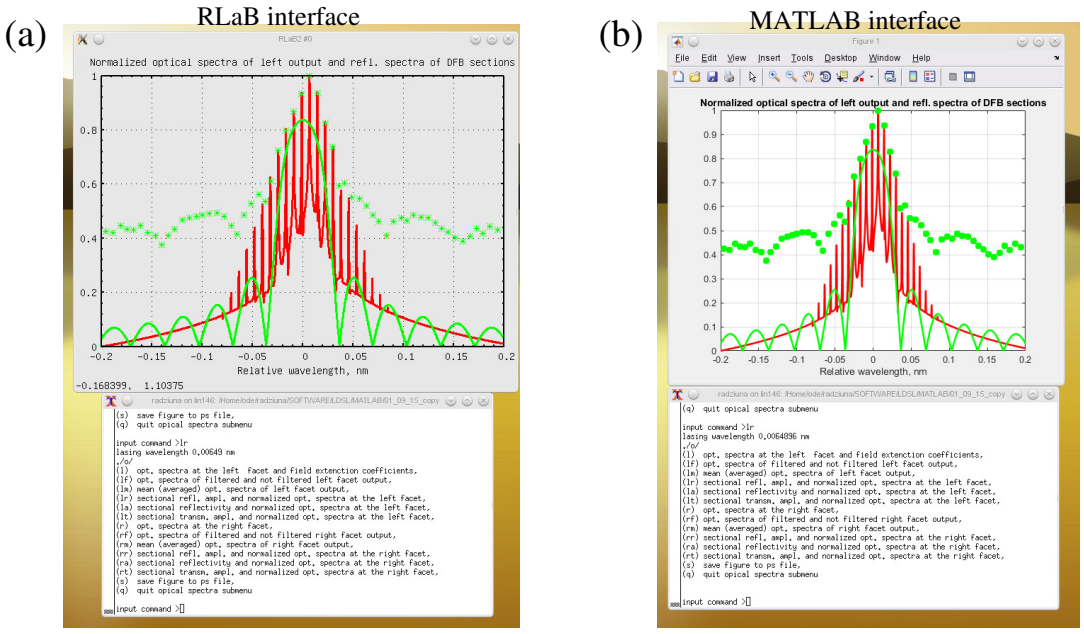

Figure 14: User environment of LDSL-tool using RLaB (a) and MATLAB executed in the command line modus (b). Top: normalized optical spectra (red curve), normalized amplitudes and wavelength of optical modes according to the mode expansion of the optical field (green symbols), and Bragg grating reflectivity spectra (green curve) in the ECDL operating at $I = 250$ mA. Bottom: command line user environment.

time has managed to translate most of the important RLaB routines into MATLAB. An example of the old RLaB-based working interface and a new MATLAB-based interface executed in the command modus are shown in Fig. 14. We note, that besides of command-modus MATLAB interface (which is identical to the old, RLaB-based interface) shown in this figure, one can also exploit more possibilities of the graphical user interface available in MATLAB.

References

[1] LDSL-tool: a software package for simulation of longitudinal dynamics in semiconductor lasers. `http://www.wias-berlin.de/software/ldsl/`

[2] E. Luvsandamdin, C. Kürbis, M. Schiemangk, A. Sahm, A. Wicht, A. Peters, G. Erbert, and G. Tränkle, "Micro-integrated extended cavity diode lasers for precision potassium spectroscopy in space," *Opt. Express*, vol. 22, pp. 7790–7798, 2014.

[3] B. Krauskopf and D.Lenstra, Eds., *Fundamental issues of nonlinear laser dynamics*. AIP Conf. Proc., vol. 548, 2000.

[4] R. Lang, and K. Kobayashi, "External optical feedback effects on semiconductor injection laser properties," *IEEE J. Quantum Electron.*, vol. 16, pp. 347–355, 1980.

[5] D. Lenstra, G. Vemuri, and M. Yousefi, “Generalized optical feedback: Theory,” in *Unlocking dynamical diversity: Optical feedback effects on semiconductor lasers*, D.M. Kane and K.A. Shore, Eds. John Wiley Sons, West Sussex, 2005, pp. 55–80.

[6] V.Z. Tronciu, H.-J. Wünsche, M. Wolfrum, and M. Radziunas “Semiconductor laser under resonant feedback from a Fabry-Perot resonator: Stability of continuous-wave operation,” *Phys. Rev. E*, vol. 73, 046205, 2006.

[7] S. Yanchuk and M. Wolfrum, “A multiple timescale approach to the stability of external cavity modes in the Lang-Kobayashi system using the limit of large delay,” *SIAM J. Appl. Dyn. Syst.*, vol. 9, pp. 519–535, 2010.

[8] U. Bandelow, M. Radziunas, J. Sieber, and M. Wolfrum, “Impact of gain dispersion on the spatio-temporal dynamics of multisection lasers,” *IEEE J. Quantum Electron.*, vol. 37, pp. 183–188, 2001.

[9] M. Radziunas, K.-H. Hasler, B. Sumpf, Tran Quoc Tien, and H. Wenzel, “Mode transitions in DBR semiconductor lasers: Experiments, simulations and analysis,” *J. Phys. B: At. Mol. Opt. Phys.*, vol. 44, p. 105401, 2011.

[10] M. Radziunas and H.-J. Wünsche, “Multisection lasers: longitudinal modes and their dynamics,” in *Optoelectronic devices – advanced simulation and analysis*, J. Piprek, Ed. Spinger Verlag, 2005, pp. 121–150.

[11] M. Radziunas, “Numerical bifurcation analysis of traveling wave model of multisection semiconductor lasers,” *Physica D*, vol. 213, pp. 98–112, 2006.

[12] M. Spreemann, M. Lichtner, M. Radziunas, U. Bandelow, and H. Wenzel, “Measurement and simulation of distributed-feedback tapered master-oscillators power-amplifiers,” *IEEE J. Quantum Electron.*, vol. 45, pp. 609–616, 2009.

[13] V.Z. Tronciu, M. Radziunas, Ch. Kürbis, H. Wenzel, and A. Wicht, “Numerical and experimental investigations of micro-integrated external cavity diode lasers,” *Optical and Quantum Electron.*, vol. 47, pp. 1459–1464, 2015.

[14] M. Radziunas, V.Z. Tronciu, E. Luvsandamdin, Ch. Kürbis, A. Wicht, and H. Wenzel, “Study of micro-integrated external-cavity diode lasers: simulations, analysis and experiments,” *IEEE J. Quantum Electron.*, vol. 51, p. 2000408, 2015.

[15] M. Radziunas, “A multi-mode delay differential equation model for lasers with optical feedback,” *An extended abstract accepted to NUSOD conference*, 2016.

[16] M. Radziunas, H.-J. Wünsche, B. Krauskopf, and M. Wolfrum, “External cavity modes in Lang-Kobayashi and traveling wave models,” *SPIE Proceedings Series*, vol. 6184, p. 61840X, 2006.

[17] A.G. Vladimirov and D. Turaev, “Model for passive mode-locking in semiconductor lasers,” *Phys. Rev. A*, vol. 72, p. 033808, 2005.